





# Stoichiometric balancing of bismuth ferrite-perovskite nanoparticles: comparative investigations on biogenic versus conventional chemical synthesis

S. Jasmine Jecintha Kay<sup>1</sup>, N. Chidhambaram<sup>1,\*</sup> , Arun Thirumurugan<sup>2</sup>, Shajahan Shanavas<sup>3</sup>, P. Sakthivel<sup>4</sup> , and R. S. Rimal Isaac<sup>5</sup>

<sup>1</sup> Department of Physics, Rajah Serfoji Government College (Autonomous) [Affiliated to Bharathidasan University], Thanjavur, Tamil Nadu 613005, India

<sup>2</sup> Sede Vallenar, Universidad de Atacama, Av. Costanera #105, Vallenar 1612178, Chile

<sup>3</sup> Research & Innovation Center for Graphene and 2D Materials, Khalifa University of Science and Technology, P.O. Box 127788, Abu Dhabi, United Arab Emirates

<sup>4</sup> Department of Physics, Science and Humanities, Centre for Materials Science, Faculty of Engineering, Karpagam Academy of Higher Education, Coimbatore, Tamil Nadu 641021, India

<sup>5</sup> Department of Nanotechnology, Noorul Islam Centre for Higher Education (Deemed to be University), Kumaracoil, Kanyakumari, Tamil Nadu 629180, India

**Received:** 18 July 2023

**Accepted:** 16 October 2023

**Published online:**  
26 October 2023

© The Author(s), under exclusive licence to Springer Science+Business Media, LLC, part of Springer Nature, 2023

## ABSTRACT

This work signifies the comparative study of physicochemical features of perovskite bismuth ferrite (P-BiFeO<sub>3</sub>) nanoparticles synthesized via the chemical coprecipitation and *Azadirachta indica* (neem)-mediated biogenic methods. The X-ray diffraction analysis of the P-BiFeO<sub>3</sub> corroborates the biogenic (B-BFO) sample requires no non-stoichiometric compensation, whereas the chemical (C-BFO) sample experiences volatile bismuth nitrate compensation. The C-BFO and B-BFO samples exhibit bandgap values of 2.14 and 2.10 eV, respectively. The strong bonds related to P-BiFeO<sub>3</sub> and the existence of alkanes and aldehydes of C-H bonds in the green-mediated sample were confirmed using FTIR spectroscopy. X-ray photoelectron spectroscopy study confirms that the Bi and Fe elements exist in the 3<sup>+</sup> valence state in the P-BiFeO<sub>3</sub>, which is of 3:3 perovskite type in both samples. The FESEM analysis of B-BFO and C-BFO samples reveals sporadic-spherical shape morphology. The B-BFO and C-BFO samples, in an applied magnetic field, at room temperature display weak ferromagnetism. The production of perovskite BiFeO<sub>3</sub> via the biogenic approach will pave the way for next-level clean practical devices.

Address correspondence to E-mail: nchidambaraselvan@gmail.com

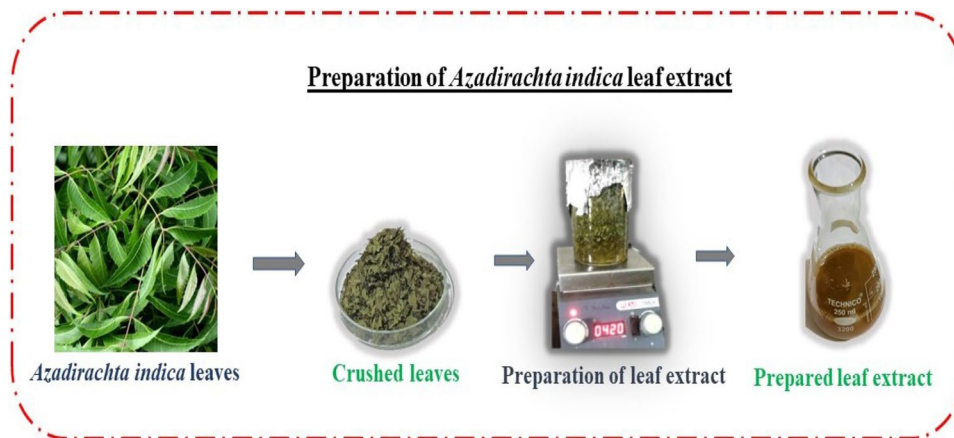
<https://doi.org/10.1007/s10854-023-11486-4>

## 1 Introduction

In the recent past, indagation has focused deeply on nanomaterials that display both magnetic and electrical ordering. If magnetic and electric order can be jointly controlled, the correlation between magnetic and electric qualities can enable the development of innovative technologies [1]. At ambient temperature, P-BiFeO<sub>3</sub> is one such multiferroic material that simultaneously displays magnetic and electric types of ordering, and the investigation into these materials is very active even in the current trend [2]. It is, thus, a potentially promising material for use in detectors, dynamic RAM, microactuators, and nonvolatile ferroelectric RAM [3]. A material that possesses more than one ferroic feature like ferromagnetism, ferrotoroidicity, ferroelasticity, and ferroelectricity in the single phase is said to be multiferroic, today the concept of multiferroics has been enlarged to include other long-range orders, such as antiferromagnetism [4]. Due to their low cost, wide availability, and stability, ferroelectric materials are particularly advantageous to ferroelectric photovoltaic devices in practical applications [5]. A well-known multiferroic distorted-rhombohedral P-BiFeO<sub>3</sub> with space group of R3c at room temperature exhibits G-order antiferromagnetic with the Neel temperature below 370 °C and ferroelectric characteristics with 830 °C Curie temperature, concurrently and in the same state. While magnetism is hypothesized to emerge from the half-filled *d* orbital of Fe ions, the ferroelectricity is ascribed to the un-shared electrons in the 6s<sup>2</sup> orbital of the Bi<sup>3+</sup> ions. Bulk BiFeO<sub>3</sub> features antiferromagnetic properties due to its spiral spin form, which has a period of ~ 62 nm [6]. These materials have numerous useful applications such as data storage, sensors, magnetoelectric memories, ferromagnetic resonance, photocatalysts, spin valves, photovoltaic systems, and spintronic devices [7–10]. Due to the considerable interest in P-BiFeO<sub>3</sub>, many preparation methods have been explored to date, including the Pechini process, coprecipitation method, rapid liquid sintering, mechanical activation, and sol–gel process among other wet-chemical and mechanical procedures [2, 11, 12] Nevertheless, each of these strategies has advantages and disadvantages of its own. Leading to the generation of secondary phases like Bi<sub>25</sub>FeO<sub>40</sub> and Bi<sub>2</sub>Fe<sub>4</sub>O<sub>9</sub>, the preparation of pure P-BiFeO<sub>3</sub> is difficult [13]. In

the investigation of BiFeO<sub>3</sub> electrodes employing the electrodeposition method, Vijaykumar V. Jadhav et al. reported peaks corresponding to Bi<sub>2</sub>F<sub>4</sub>O<sub>9</sub> and Bi<sub>25</sub>FeO<sub>40</sub>, even at 600 °C [4]. Sushmita Ghosh et al. prepared BiFeO<sub>3</sub> via metal complex powder method temperature ranging from 400 to 600 °C by using nitric and tartaric acids as chelating agents, they noticed secondary phases like Bi<sub>25</sub>FeO<sub>40</sub> and Bi<sub>2</sub>Fe<sub>4</sub>O<sub>9</sub> [14]. K. Prashanthi et al. fabricated BiFeO<sub>3</sub> nanowires utilizing the sol–gel method, and the presence of Bi<sub>2</sub>Fe<sub>4</sub>O<sub>9</sub> was evident from their results, they also concluded that the stoichiometric deficiency of volatile Bi led to the formation of Bi<sub>2</sub>Fe<sub>4</sub>O<sub>9</sub> [15]. For such pure-phase preparation of BiFeO<sub>3</sub>, the wet-chemical approach is plausible. Coprecipitation is ideal since it can create homogenous nanosized particles quickly and economically. Lower bismuth evaporation temperatures are one of the challenges in the synthesis of BiFeO<sub>3</sub>; however, this issue can be addressed and the development of secondary phases during the reaction might also be prevented by using the coprecipitation approach [2]. Currently, a fascinating area of nanoscience is the synthesis of metal nanoparticles through biogenic approaches. During the Rio Conference's organizing, the idea of cleaner production emerged (UN, 1992). Cleaner production is defined by UNEP (United Nations Environmental Program) as "the ongoing application of an integrated preventive environmental strategy to processes, products, and services to boost productivity and lowering risks to humans and the environment" (UNEP, 1991). It was created, using concepts from the 3P (pollution prevention pays) paradigm intending to reduce the environmental effect of industry [16]. As a consequence, plant-mediated biosynthesis has drawn more consideration as a cost-effective, simple, efficacious, and realizable way; in addition, it is a great proxy for traditional processing techniques to nanoparticle synthesis [17]. This work intends to compare the structural, optical, and magnetic features of P-BiFeO<sub>3</sub> in the chemical coprecipitation method and the *Azadirachta indica* (neem)-mediated biogenic method. The synthesis of conventional nanomaterials, either by physical or chemical synthesis, has unintended consequences for the environment and human health, which have been linked to the depletion of resources, climate variability, environmental consequences, and human health issues, whereas in the developing discipline of "biogenic synthesis,"

**Fig. 1** *Azadirachta indica* leaf extract preparations



nanomaterial production is being developed and improved in a way that is efficient, safe, sustainable, clean, and environmentally beneficial. By using nature-abundant materials as synthesis reagents, clean nanomaterials can be synthesized [18]. *Azadirachta Indica*, popularly referred to as neem, is a species of the Meliaceae family, which is mostly prevalent in several Asian nations. The entire tree can be used for traditional medicine or a variety of therapeutic purposes. *Azadirachta indica* has green petiolate, unpaired leaflets that are alternating and have seven to nine leaflets [19, 20]. The primary phytochemicals like ketones, flavones, aldehydes, organic acids, and amides exist in *Azadirachta indica* extract which acts as bio-reductants. Of these, organic acids, flavones, and quinones are water-dissoluble phytonutrient that are accountable for the efficient transformation of metal ions into the appropriate nanostructures. These bio-organic substances are known to be vital in the nanoparticles formations as either stabilizing or reducing agents. It is considered that the electrostatic or ionic interactions between the metal complexes and the phytochemicals exist in the extract contribute to the formation of nanoparticles [21]. Additionally, using green materials is in line with the environmental firm's societal shift in favors of using natural solutions [22]. As far as we are aware, P-BiFeO<sub>3</sub> has not yet been synthesized via *Azadirachta indica* extract and compared with chemically synthesized bismuth ferrite. Motivated from the above-mentioned discussion, P-BiFeO<sub>3</sub> nanoparticles have been synthesized using the biogenic approach and explored their physio-chemical properties. Further, P-BiFeO<sub>3</sub> nanoparticles are also synthesized by chemical approach

so as to compare their physio-chemical properties with biogenic-derived nanoparticles.

## 2 Experimental

### 2.1 Preparation of bio-extricate

The foliage of *Azadirachta indica* was collected from the surroundings of Thanjavur. The foliage was well gutted with distilled water, allowed to dry completely, and pulverized. Thereafter, 10 g of pulverized foliage was added to 100 mL of distilled water and boiled at 80 °C for an hour under incessant magnetic stirring, and the resultant solution was cooled in ambient temperature. After that, the sediments were filtered out via Whatman No.1 filter paper, and the concentrated extract, thus, procured was retained for future use and used as a cross-linking agent to produce perovskite bismuth ferrite. Figure 1 shows the pictorial representation of the preparation of the *Azadirachta indica* leaf extract.

### 2.2 Biogenic synthesis of BiFeO<sub>3</sub> (B-BFO)

In a typical synthesis process, in 50 mL of concentrated foliage extract, 4.996 g of bismuth nitrate pentahydrate and 4.04 g of iron nitrate nonahydrate were added at intervals of 15 min to one another. To compensate for the volatility of bismuth nitrate throughout the experiment, an additional 3% of bismuth was added [2]. After the complete dissolving of the starting materials, the mixture was held in reserve at 80 °C for 2 h. The consequential blackish-brown solution was allowed to settle overnight, although no precipitation was found.

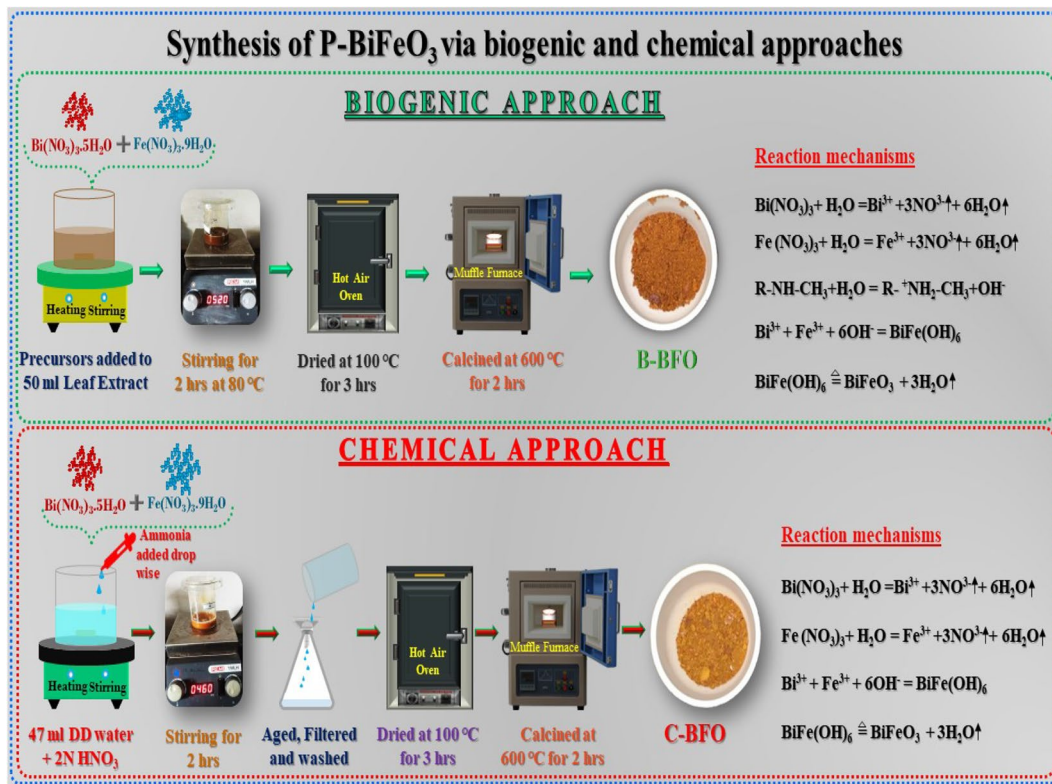


**Fig. 2** Schematic of P-BiFeO<sub>3</sub> synthesis via biogenic (B-BFO) and chemical (C-BFO) approaches

The mixture was dried in an oven at 100 °C for about 3 h. The ensuing powder after drying was calcined at 600 °C in a muffle furnace for 2 h to ensure their crystallization. The obtained reddish-brown color product was labeled as B-BFO nanoparticles. Figure 2 illustrates the schematic of the synthesis and reaction mechanism of the biogenic B-BFO approach.

### 2.3 Chemical synthesis of BiFeO<sub>3</sub> (C-BFO)

Inorganic perovskite bismuth ferrite was synthesized using the chemical coprecipitation method. At a short interval of time between one another, the stoichiometric ratio (1.03:1, i.e., 4.996 and 4.04 g) of metal precursors such as bismuth nitrate pentahydrate and iron nitrate nonahydrate was added to 47 mL of de-ionized water along with 3 mL of HNO<sub>3</sub> as a leaching agent [23] at room temperature. The reason for adding an additional 3% of bismuth precursor is to account for the volatile nature of bismuth nitrate. After complete homogenization of metal precursors, the concentrated ammonia solution was gradually dripped into the solution until the pH attained 9. The as-obtained precipitated solution was continuously stirred for another

2 h. The mixture was allowed to rest overnight, and the obtained precipitate was filtered and washed till the pH reached 7. The resultant precipitate was then held in an oven at 100 °C for 3 h to evaporate the residual moisture. Subsequently, the obtained blackish-brown powder was further calcined at 600 °C in a muffle furnace for 2 h yielding golden-brown bismuth ferrite nanopowders labeled as C-BFO. Figure 2 illustrates the schematic of the synthesis and reaction mechanism of the biogenic C-BFO approach.

### 2.4 Characterizations

Structural analysis of the synthesized B-BFO and C-BFO nanoparticles was analyzed utilizing an X-ray diffractometer (PANalytical-PW3040/60X'pert PRO) utilizing Cu-K $\alpha$  irradiation spanned across 20° to 80° in 2 $\theta$  mode. Utilizing Bruker Topaz version 6, the Rietveld refinement analysis was performed for quantitative analysis. The reflectance spectra were recorded using a Varian-Cary 5000 spectrophotometer. The chemical bonding of the B-BFO and C-BFO nanoparticles was investigated by Perkin Elmer BX-II Fourier transform infrared (FTIR) spectroscopy in



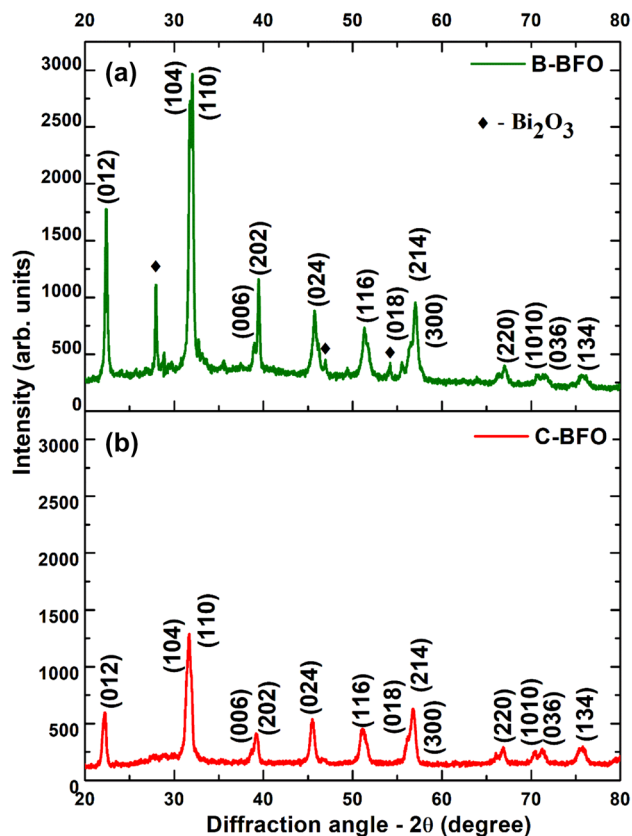


**Fig. 3** XRD patterns of **a** biogenic (B-BFO) and **b** chemically (C-BFO) synthesized bismuth ferrite nanoparticles

the wavenumber of  $4000\text{--}400\text{ cm}^{-1}$  by the KBr pellet technique. A PHI5000 Versa Probe II (ULVAC-PHI) XPS Photoelectron spectroscopy with an Al  $K\alpha$  X-ray source was employed to measure the XPS spectra of both samples. The morphology and structure of the prepared nanoparticles were examined by Thermofisher Quanta FEG250 Field Emission Scanning Electron Microscopy (FESEM). The magnetic characteristics of the prepared samples were investigated by utilizing a Lakeshore 7400-5 series vibrating sample magnetometer (VSM).

### 3 Results and discussions

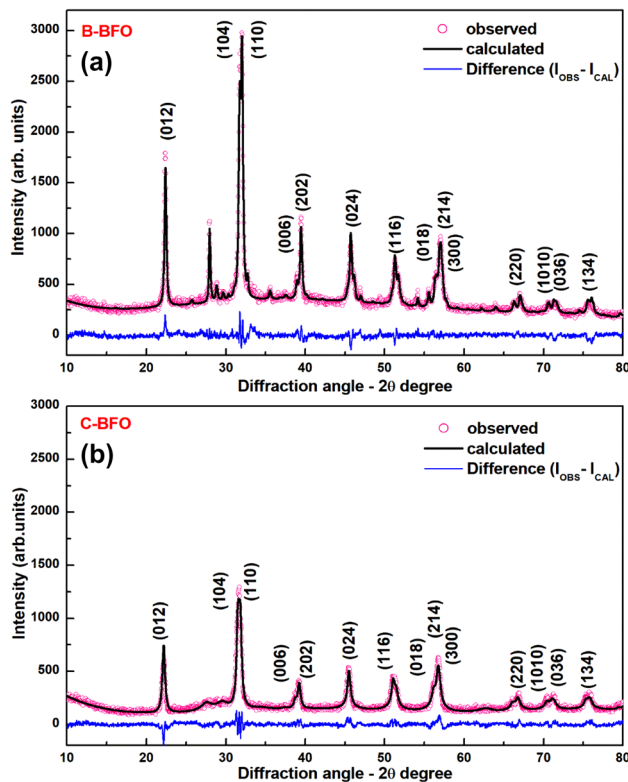
#### 3.1 XRD analysis

Figure 3a, b exhibits the XRD diffraction patterns of B-BFO and C-BFO-synthesized bismuth ferrite, respectively. The noticed diffraction pattern compliance with the rhombohedral  $\text{BiFeO}_3$  perovskite having R3c space group of JCPDS card No. 01-071-2494

[11] for both samples. The peaks are indexed as (012), (104), (110), (202), (024), (116), (018), (214), (300), (220), (1010), (036), and (134) which corresponds to the phase pure bismuth ferrite. The phase purity of both the  $\text{BiFeO}_3$  samples was identical. While the C-BFO sample lacks any additional peaks, the B-BFO sample does contain a few frail impurity peaks of  $\text{Bi}_2\text{O}_3$  (indicated by  $\blacklozenge$ ) in Fig. 3a. This affirms that although we used similar precursor ratios for both samples as mentioned in the “experimental” section (i.e., 3% extra bismuth nitrate to compensate for its volatility during the experiment), the B-BFO sample requires no compensation whereas the C-BFO sample experienced volatile bismuth nitrate compensation. Since bismuth has a low melting point and is subjected to extreme temperatures during synthesizing, this generates a high vapor pressure, which makes it volatile. For synthesizing pristine stoichiometric  $\text{BiFeO}_3$ , the volatility of bismuth can be an issue.  $\text{Bi}_2\text{Fe}_4\text{O}_9$  and  $\text{Bi}_2\text{FeO}_{40}$  are two stable auxiliary phases that can occur as a result of bismuth’s volatility, which is in charge of significant leakage currents and low electrical resistivity, which were absent in both of the samples [2, 24]. This implies the phase purity of both samples. The intensity of the diffraction peaks of green bismuth ferrite upsurges in juxtaposition with chemically synthesized bismuth ferrite along with the decrease in the peak half-width. This implies that the particle size has grown [12]. A further indication of the rhombohedral distortion of the  $\text{BiFeO}_3$  perovskite is seen by the splitting of the  $39^\circ$  and  $57^\circ$  peaks in both samples, it is also evident from XPS spectra [25]. By measuring the full-width half maximum of the diffraction peaks of bismuth ferrite in both cases and applying Scherrer’s formula [26], the average crystallite size ( $D$ ) of the synthesized B-BFO and C-BFO samples was estimated.

$$D = \frac{K\lambda}{\beta \cos\theta}, \quad (1)$$

where  $\lambda$  is the wavelength of the X-rays of value  $1.5406\text{ \AA}$ ,  $\beta$  denotes full-width half maximum, after the error due to instrumental broadening,  $K$  denotes the Scherrer constant (0.9), and  $\theta$  gives Bragg’s diffraction angle [27, 28]. The estimated average crystallite sizes are 63 and 37 nm for the B-BFO and C-BFO samples, respectively. The Rietveld refinement was used to analyze the XRD data quantitatively, and Fig. 4 displays the observed, calculated, and differences



**Fig. 4** Refined XRD profiles of **a** biogenic (B-BFO) and **b** chemically (C-BFO) synthesized bismuth ferrite nanoparticles

in the refinement of the samples. The refined lattice parameters are tabulated in Table 1. Using the rhombohedral crystal structure with the space group R3c, the refinement was carried out [29]. The low values of the fitting qualities show a good refinement of both samples. From Rietveld refinement weight percentages, it is palpable that the B-BFO sample entails on no account non-stoichiometric compensation while the C-BFO sample involves volatile bismuth nitrate compensation. The linear attenuation coefficient and crystal density of the B-BFO sample seem marginally lower than the C-BFO sample might be the presence of secondary  $\text{Bi}_2\text{O}_3$  phases.

### 3.2 UV–Vis analysis

Figure 5 depicts the DRS spectra of the synthesized B-BFO and C-BFO samples in a range of 400–800 nm. The UV–Vis DRS spectra of both samples display an effective absorption between 400 and 525 nm and a modest absorption between 600 and 800 nm. An intense transition is observed in the region of 500–600 nm, which correlates with charge transfer owing to electronic conversion from valence band levels— $\text{O}_{2p}$  to conduction band levels— $\text{Fe}_{3d}$ . There are two distinctive reflection regions in the spectra. One of them is in the region between 500 and 700 nm which corresponds to metal–metal transitions, while the other is betwixt 700–800 nm and is attributed to crystal field transitions [30]. To appraise the optical bandgap ( $E_g$ ) of both samples, Tauc’s plot was plotted between  $F(R)hv^2$  and the energy of photons ( $hv$ ). Moreover, the related Kubelka–Munk (K–M) function is expressed as follows:

$$F(R) = \frac{(1 - R)^2}{2R}, \quad (2)$$

$$F(R)hv = (hv - E_g)^n, \quad (3)$$

where  $F(R)$  is the K–M function,  $h$  is Planck’s constant,  $R$  is the reflectance,  $\nu$  is the frequency,  $(1-R)^2/2R$  is the absorption coefficient, and ‘ $n$ ’ value rests on the type of transition ( $n = 2$  and  $1/2$  for indirect and direct transitions, respectively) [31]. The calculated bandgap values for C-BFO and B-BFO samples remain at 2.14 and 2.10 eV, respectively (inset of Fig. 5). The results are well in line with past literature reports [32–34]. In comparison to the C-BFO, the B-BFO has a narrow band gap value and lacks a distinctive reflection edge in the 700–800 nm range. These results provide a comprehension of the influence of the secondary phase on the optical characteristics of B-BFO. It is evident from the XRD study that only this sample contained

**Table 1** Refined structural parameters of B-BFO and C-BFO nanoparticles

Sample	Lattice parameters (Å)		Volume of unit cell V (Å <sup>3</sup> )	Space group	Crystal linear absorption coeff. (1/cm)	Crystal density (g/cm <sup>3</sup> )	Phase percentage	Goodness of fit
	$a=b$	$c$						
B-BFO	5.5820 (5)	13.8730 (15)	374.35 (8)	R3c	1761.3 (7)	8.308 (4)	BiFeO <sub>3</sub> –89.8% Bi <sub>2</sub> O <sub>3</sub> –10.2%	1.34
C-BFO	5.5875 (10)	13.875 (3)	375.15 (16)	R3c	1765.1 (4)	8.3257 (19)	BiFeO <sub>3</sub> –100%	1.38

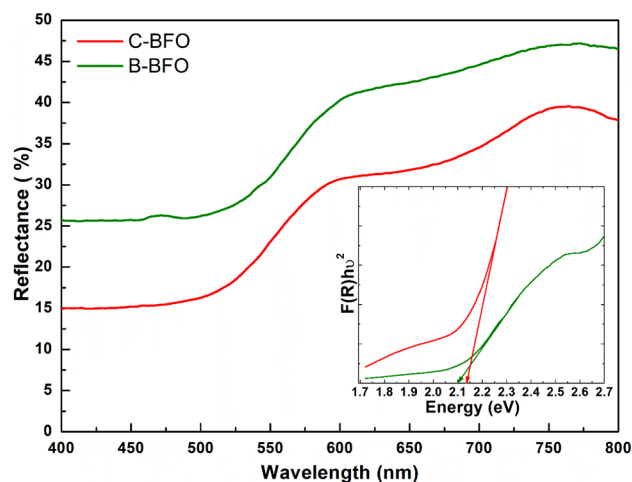


**Fig. 5** UV–Vis diffuse reflectance spectra (DRS) of biogenic (B-BFO) and chemically (C-BFO) synthesized bismuth ferrite nanoparticles (Inset displays Tauc's plot of both samples)

the secondary phase, and the secondary phase could be associated with the lower band gap of the B-BFO [35]. As a result of the metal–metal transition between the  $\text{BiFeO}_3\text{--Bi}_2\text{O}_3$  scheme, the reflection in the range between 500 and 700 nm could have been affected, drastically lowering the optical bandgap energy of B-BFO. The occurrence of defect-induced energy states amid the valence and conduction bands, and especially energy states near the conduction band, could also lower bandgap energy. Since the crystal field strength is correlated to the crystal structure and has a significant impact on the position of the crystal field transition edge, the reflection edge between 700 and 800 nm is unnoticed in B-BFO [12].

### 3.3 FTIR analysis

The infrared spectra of the C-BFO and B-BFO samples in transmission mode over the range of wavenumbers 4000 to  $400\text{ cm}^{-1}$  are represented in Fig. 6. The as-prepared samples exhibit two absorption peaks in the array of  $400\text{--}700\text{ cm}^{-1}$ . The bands at  $438$  and  $555\text{ cm}^{-1}$  correspond to the Fe–O–Fe bending and stretching mode vibrations along the Fe–O axis, respectively, which signifies the features of the  $\text{FeO}_6$  octahedra assemblies in the perovskites [23]. The vibrational mode of  $\text{BiO}_6$  octahedra is observed at  $423\text{ cm}^{-1}$ . The vibrational band around  $519\text{ cm}^{-1}$  is ascribed to the overlapping of bending and stretching vibrations of both Bi–O and Fe–O, a trait that specifies P- $\text{BiFeO}_3$

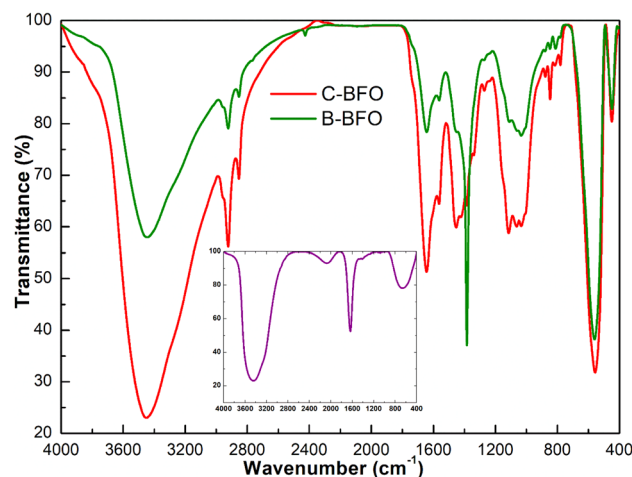


**Fig. 6** FTIR spectra of biogenic (B-BFO) and chemically (C-BFO) synthesized bismuth ferrite nanoparticles (Inset shows FTIR spectrum of *Azadirachta indica* leaf extract)

with the R3c structure, this indicates the presence of bismuth ferrite. [29, 36]. The presence of trapped nitrates on the surface causes the vibrational bands at around  $1410\text{--}800\text{ cm}^{-1}$ , particularly those at  $1390\text{ cm}^{-1}$  and  $918\text{ cm}^{-1}$ , which are induced by the stretching vibrations of  $\text{NO}_3^-$  ions in bismuth ferrite [37]. The vibrational bands noticed at  $2900$  and  $2852\text{ cm}^{-1}$  are accredited to the stretching symmetric vibrations of C–H bonds [38]. The broad bands at  $3700\text{--}3000\text{ cm}^{-1}$  and  $1670\text{--}1600\text{ cm}^{-1}$  correspond to the stretching mode of antisymmetric O–H and symmetric H–O–H assemblages, respectively [39]. There appear two distinct peaks at  $2422$  and  $1391\text{ cm}^{-1}$  in the B-BFO sample, attributed to the aliphatic stretching vibration and bending mode of alkanes and aldehydes of C–H bonds, respectively [40, 41], which are absent in the C-BFO sample. The above discussion makes clear that the biogenic-derived B-BFO has characteristic functional groups of bismuth ferrite with those of chemically derived C-BFO, negating the necessity of using harmful reducing agents to prepare bismuth ferrite nanoparticles.

### 3.4 XPS analysis

X-ray photoelectron spectroscopic investigations were carried off at ambient temperature to ascertain the valence state of the ions for C-BFO and B-BFO samples (Figs. 7 and 8). Figures 7a and 8a demonstrate the wide survey spectrum of C-BFO and



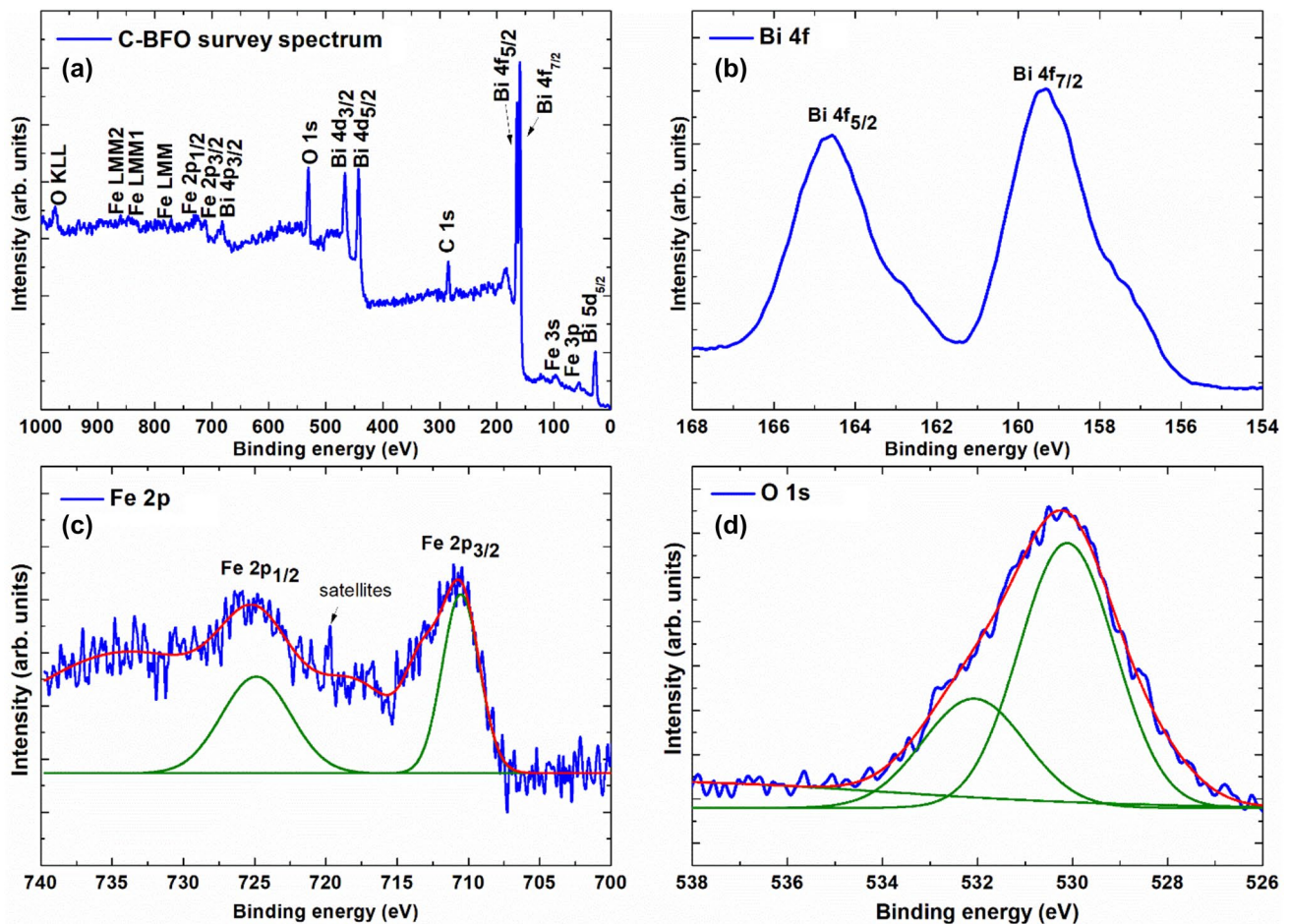


**Fig. 7** **a** XPS survey spectrum of C-BFO nanoparticles, **b** high-resolution spectrum of Bi 4f, **c** deconvoluted high-resolution spectrum of Fe 2p, and **d** deconvoluted high-resolution spectrum of O 1s

B-BFO samples, respectively. The obtained photoelectron peaks reveal unequivocally the presence of key elements, i.e., bismuth, iron, and oxygen. The C1s spectrum at 285 eV aided as the standardization reference for all observed spectra. The three significant elements such as Bi 4f, Fe 2p, and O 1s linked to the formation of perovskite  $\text{BiFeO}_3$  were analyzed using a narrow scan survey for both samples. Figures 7b and 8b exhibit the doublet spectra of Bi 4f for C-BFO and B-BFO samples, respectively. The doublet peaks of bismuth were found at binding energies of 158.6 eV, 163.9 eV for B-BFO and at 159.2 eV, 164.5 eV for C-BFO samples which corresponds to  $\text{Bi } 4f_{7/2}$  and  $\text{Bi } 4f_{5/2}$  peaks. Moreover, the splitting energy of doublet Bi 4f spin-orbit is 5.3 eV, which is also identical to the energy variance among the  $\text{Bi } 4f_{7/2}$  and  $\text{Bi } 4f_{5/2}$  peaks for as-synthesized samples. This indicates that there is no Bi deficit in these samples which agrees

well with the compensation in the stoichiometric composition of  $\text{BiFeO}_3$ . This affirms the intrinsic oxidation state of the Bi ions is +3 also attributed to the Bi–O bonds in the samples. This matches the values that have been previously reported from both theoretical calculations and experimental data [42]. Figures 7c and 8c illustrate the core level spectra of the Fe 2p state for C-BFO and B-BFO samples, respectively. The doublet  $\text{Fe } 2p_{3/2}$  and  $\text{Fe } 2p_{1/2}$  lines corresponding to the Fe 2p state are located at binding energies 710.25 eV, 723.8 eV for B-BFO, and at 710.8 eV, 724.6 eV for C-BFO samples. Additionally, it is revealed that  $\text{Fe } 2p_{3/2}$  and  $\text{Fe } 2p_{1/2}$  have energies oriented to the splitting of spin-orbit around 13.6 eV [43]. Typically, satellite peaks for  $\text{Fe}^{3+}$  and  $\text{Fe}^{2+}$  emerge at 8 eV and 6 eV, respectively, above  $\text{Fe } 2p_{3/2}$ . A satellite peak is visible in our samples



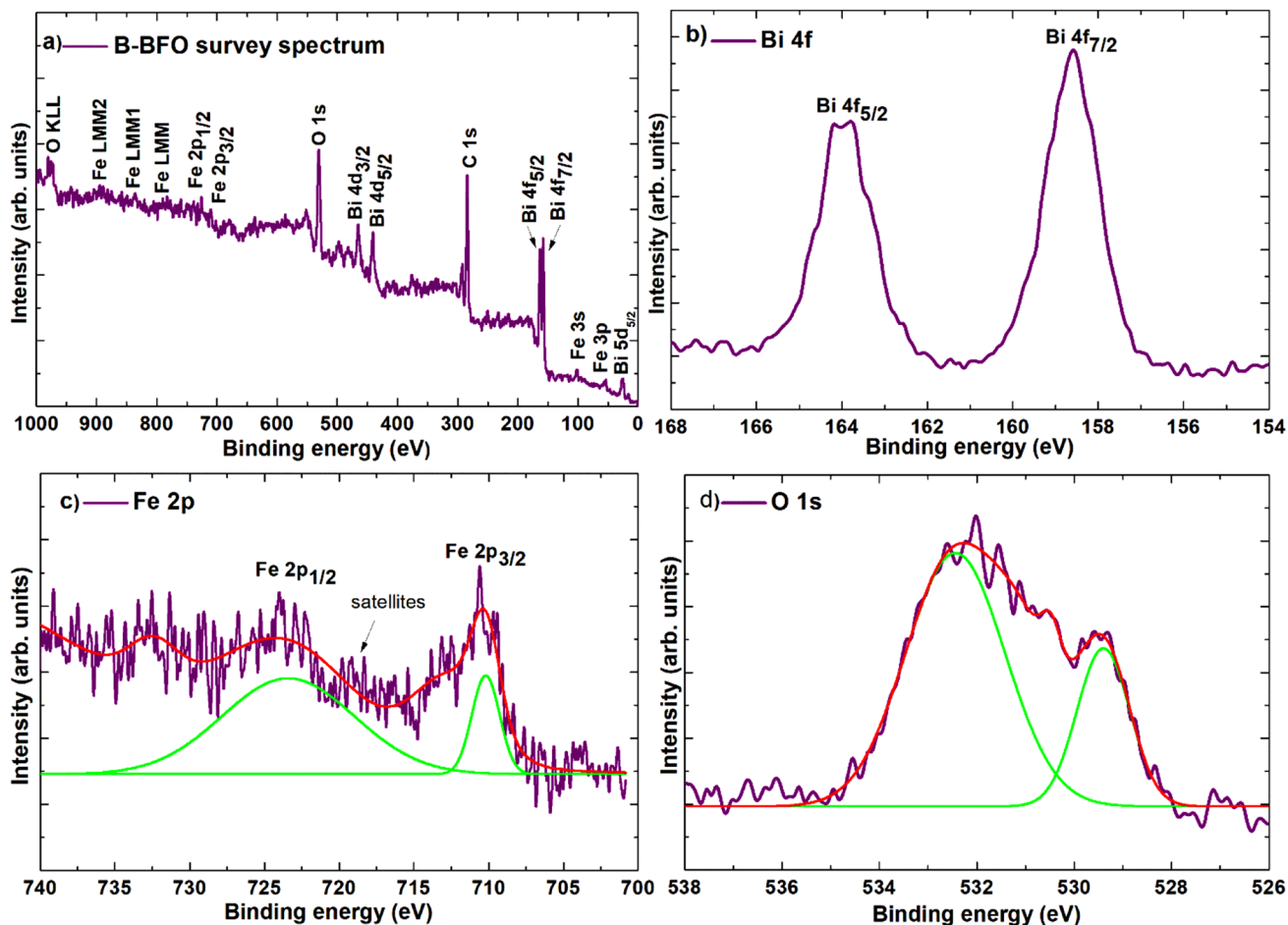


**Fig. 8** **a** XPS survey spectrum of B-BFO nanoparticles, **b** high-resolution spectrum of Bi 4f, **c** deconvoluted high-resolution spectrum of Fe 2p, and **d** deconvoluted high-resolution spectrum of O 1s

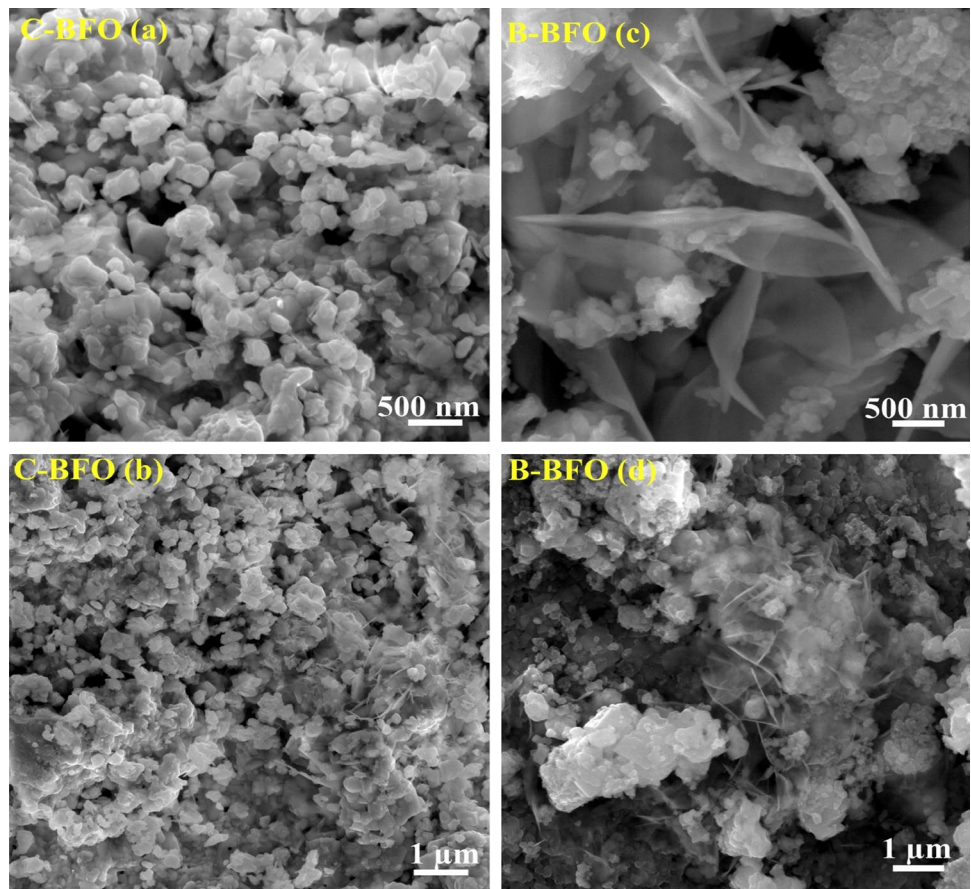
at 8 and 9 eV above Fe 2p<sub>3/2</sub> for B-BFO and C-BFO samples, respectively [35]. This further validates that the oxidation level of Fe ions is +3 in both synthesized samples. The Fe ion valences are vital in perovskite BiFeO<sub>3</sub>. While concerning, the potential devices based on BiFeO<sub>3</sub> nanomaterials are severely constrained due to their poor resilience to insulation when reduction occurs from Fe<sup>3+</sup> to Fe<sup>2+</sup> species [33]. The binding energies at 529.4 eV, 531.9 eV for B-BFO and 530.0 eV, 532.0 eV for C-BFO samples are assigned to the lattice oxygen and surface adsorbed-oxygen species, respectively (Figs. 7d and 8d). The oxygen vacancies in BiFeO<sub>3</sub> are typically caused by the presence of Fe ions in different oxidation states (Fe<sup>2+</sup>/Fe<sup>3+</sup>). The results indicate that the BiFeO<sub>3</sub> phase formed using the two approaches may be devoid of anionic or cationic defects, or they may remain well

below the threshold level of identifiable residues [44, 45].

### 3.5 FESEM analysis

Figure 9 illustrates the morphological and microstructural features of the C-BFO and B-BFO samples under different magnifications such as 500 nm and 1 μm using FESEM analysis. The morphologic characteristics of the C-BFO sample demonstrate densely agglomerated, sporadic, spherical particles with a few voids scattered across the sample surface. The morphology of the B-BFO reveals a mixture of nanoflakes and agglomerated particles with uneven shapes. The nanoflake structure of the nanomaterials might be related to the existence of a few Bi<sub>2</sub>O<sub>3</sub> impurities, which is also illustrated by XRD investigations [46]. It is generally known that agglomeration occurs because nanoparticles have high surface energies

**Fig. 9** FESEM micrographs of biogenic (B-BFO) and chemically (C-BFO) synthesized bismuth ferrite nanoparticles under 500 nm (a and c) and 1  $\mu\text{m}$  (b and d) scale bars



and a tendency to sustain themselves as roughly spherical agglomerates to have a low surface-to-volume ratio. This type of occurrence is prevalent in materials such as ferrites, oxides, and titanates [47]. Vapor pressure is higher on lighter nanoparticles than on heavier nanoparticles at high temperatures. Lighter particles evaporate besides then condense on heavier ones as a result. The attainment of a homogeneous particle size distribution in this technique is exceedingly challenging [48]. Figure 10 depicts the EDX spectra of the C-BFO and B-BFO samples. Bismuth (Bi), iron (Fe), and oxygen (O), with atomic percentages of 20.19% (Bi), 11.28% (Fe), and 68.54% (O), are all present in the elemental compositions of C-BFO nanoparticles. With atomic percentages of 11.33% (Bi), 8.75% (Fe), 51.05% (O), 27.33% (C), and 1.54% (K), the elemental compositions of B-BFO nanoparticles showed the existence of bismuth, iron, carbon, oxygen, and a frail amount of potassium. The presence of potassium (K) in B-BFO samples is due to the abundance of potassium in *Azadirachta indica* [49]. Analysis of the elemental composition of both samples exposed the existence of bismuth, iron, and oxygen.

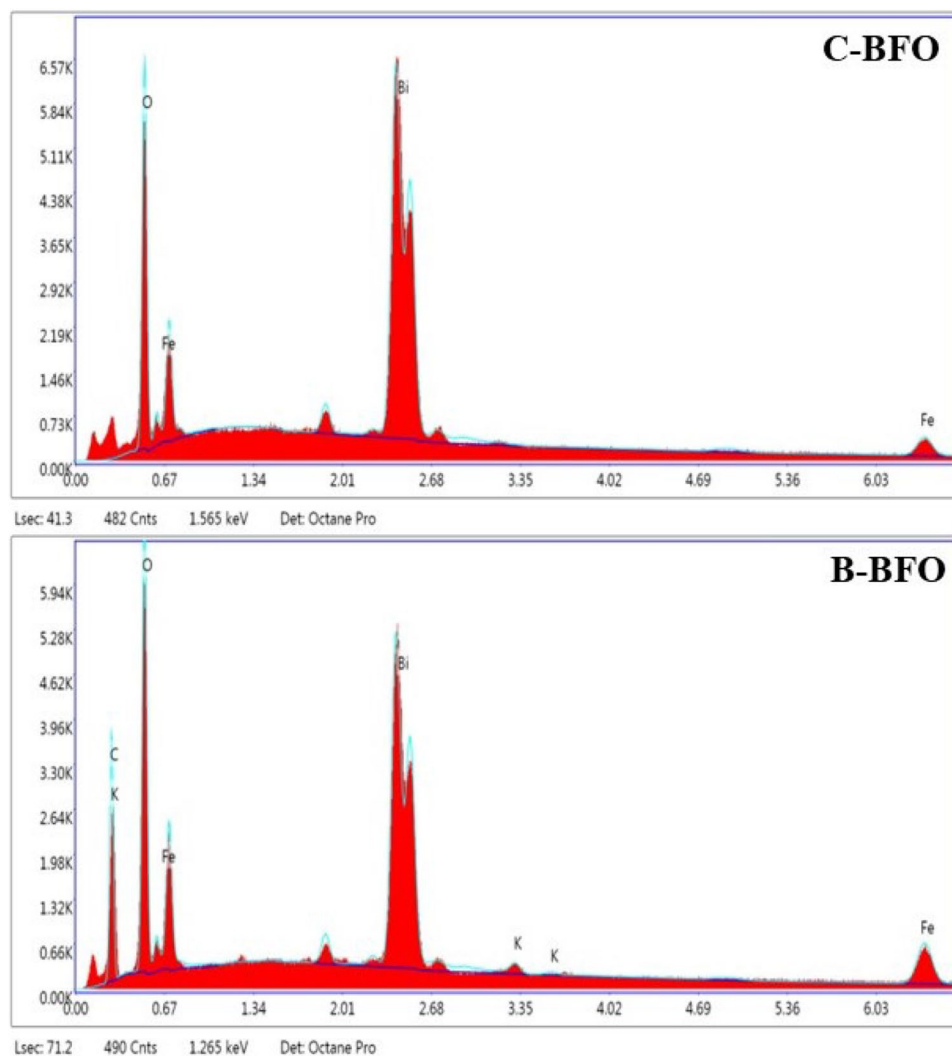
### 3.6 Magnetic analysis

Figure 11 displays the M–H curve obtained at room temperature for the synthesized samples. Both samples exemplify weak ferromagnetism. This is associated with the high surface-to-volume ratio, which enhances the palpable impact to the particle's average magnetization through indigent spins at the interfaces and forms a ferromagnetic shell [50]. The retentivity, coercivity, and maximum magnetization values from the M–H plots of the B-BFO and C-BFO samples are illustrated in Table 2. The significant values of magnetic parameters reflect the ferromagnetic behavior of the prepared samples at room temperature.

## 4 Conclusions

P-BiFeO<sub>3</sub> was synthesized via two distinct methods, chemical coprecipitation and biogenesis approaches. The green synthesis of P-BiFeO<sub>3</sub> allows us to avoid the toxic chemical agents of chemical coprecipitation.

**Fig. 10** EDX spectrum of biogenic (B-BFO) and chemically (C-BFO) synthesized bismuth ferrite nanoparticles



Aside from its reducing properties, *Azadirachta indica* leaf extract also contains some phytochemicals that are used as stabilizing agents for nanoparticles. XRD investigations of both samples show the rhombohedral structure of the R3c space group, yet B-BFO displays an increase in the intensity of reflection peaks when related to C-BFO. For the B-BFO and C-BFO samples, the mean crystallite size was estimated using Scherer's formula to be 63 and 37 nm, respectively. Similar precursor ratios (1.03:1–Bi: Fe) were employed for both samples, but the B-BFO sample does not require compensation while the C-BFO sample does require compensation for volatile bismuth nitrate during the experiment. Rietveld analysis corroborates rhombohedral structure with the R3c space group for both samples and the lattice parameters determined from the Rietveld

refinement were ( $a = b = 5.5820$  nm,  $c = 13.8730$  nm) and ( $a = b = 5.5875$  nm,  $c = 13.875$  nm) for B-BFO and C-BFO samples, respectively. The obtained band gap energies with a direct electronic transition for B-BFO and C-BFO samples are 2.14 and 2.10 eV, respectively. The FTIR studies of both samples revealed the occurrence of Fe–O and Bi–O bonds. The validity of elements with native oxidation states, as such in a stoichiometric P-BiFeO<sub>3</sub> phase, was substantiated by XPS experiments that indicated the typical binding energies of the relevant elements. The agglomerated sporadic-spherical structure is observed in the C-BFO sample, but the B-BFO sample has a mix-up form of the agglomerated sporadic-spherical structure and just a few nanoflakes due to the presence of Bi<sub>2</sub>O<sub>3</sub>. Energy-dispersive spectroscopy was used to determine the atomic percent of bismuth, oxygen,

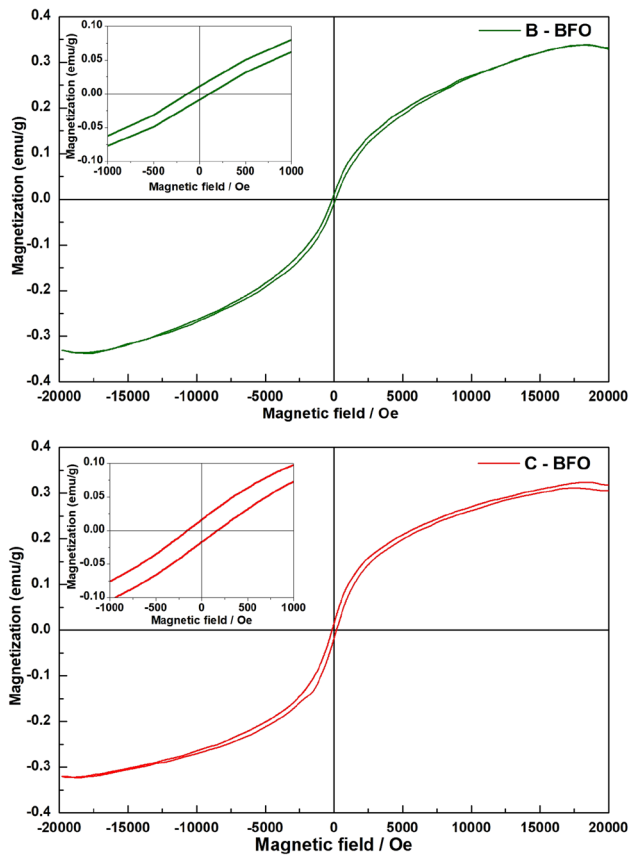


**Fig. 11** M–H plots of biogenic (B-BFO) and chemically (C-BFO) synthesized bismuth ferrite nanoparticles at room temperature (inset displays the lower field M–H plots at room temperature)

**Table 2** Magnetic parameters of B-BFO and C-BFO nanoparticles

Sample	Coercivity ( $M_c$ ) Oe	Retentivity ( $M_r$ ) emu/g	Maximum magnetization ( $M_s$ ) emu/g
B-BFO	118.62	0.011	0.33
C-BFO	156.57	0.016	0.32

and iron elements in both samples. This validates the presence of elements such as bismuth, oxygen, and iron in B-BFO and C-BFO. The magnetic properties of both samples manifest weak ferromagnetism at room temperature. It is possible to create clean nanomaterials using a biogenic method, which makes use of natural resources that are both stabilizing and reducing agents with shape and size-controlled nanoparticles. This entails bringing laboratory-based

work up to an industrial scale as well. There will be a decrease in adverse environmental contaminants if bio-mediated technological nanomaterials are used in the industries.

## Acknowledgements

The author S. Jasmine Jecinta Kay acknowledges the financial support given by the Directorate of Collegiate Education, Government of Tamil Nadu. The author S. Shanavas is grateful to Khalifa University of Science and Technology for supporting this study under CIRA-2020-085.

## Author contributions

All authors contributed to the study conception and design. Material preparation, data collection, and analysis were performed by SJJK and NC. The first draft of the manuscript was written by SJJK and all authors commented on previous versions of the manuscript. All authors read and approved the final manuscript.

## Data availability

Data will be made available on request.

## Declarations

**Conflict of interest** The authors declare no conflict of interest.

## References

1. N.V. Srihari, K.B. Vinayakumar, K.K. Nagaraja, *Coatings* **10**, 1221 (2020)
2. H. Maleki, M. Haselpour, R. Fathi, *J. Mater. Sci.: Mater. Electron.* **29**, 4320 (2018)
3. W. Gao, Y. Zhu, Y. Wang, G. Yuan, J.-M. Liu, *J. Materiomics.* **6**, 1 (2020)
4. V.V. Jadhav, M.K. Zate, S. Liu, M. Naushad, R.S. Mane, K.N. Hui, S.-H. Han, *Appl. Nanosci.* **6**, 511 (2016)



5. G. Chen, J. Chen, W. Pei, Y. Lu, Q. Zhang, Q. Zhang, Y. He, *Mater. Res. Bull.* **110**, 39 (2019)
6. S. Chandel, P. Thakur, S.S. Thakur, A. Sharma, J.-H. Hsu, M. Tomar, V. Gupta, A. Thakur, *Mater. Chem. Phys.* **204**, 207 (2018)
7. A. Roy, R. Gupta, A. Garg, *Adv. Cond. Matter. Phys.* **2012**, 1 (2012)
8. X.J. Xi, S.Y. Wang, W.F. Liu, H.J. Wang, F. Guo, X. Wang, J. Gao, D.J. Li, *J. Magn. Magn. Mater.* **355**, 259 (2014)
9. N. Wang, X. Luo, L. Han, Z. Zhang, R. Zhang, H. Olin, Y. Yang, *Nano-Micro Lett.* **12**, 81 (2020)
10. R.K. Mansingh, R.K. Mishra, T. Dash, *AIP Conf. Proc.* **2417**, 020021 (2021)
11. J. Peñalva, A. Lazo, *J. Phys.: Conf. Ser.* **1143**, 012025 (2018)
12. M. Sakar, S. Balakumar, P. Saravanan, S.N. Jaisankar, *Mater. Res. Bull.* **48**, 2878 (2013)
13. L. BAO, X. QI, R. MEI, X. CHEN, *J. Ceram. Soc. Jpn.* **126**, 372 (2018)
14. S. Ghosh, S. Dasgupta, A. Sen, H. Sekhar, Maiti, *J. Am. Ceram. Soc.* **88**, 1349 (2005)
15. K. Prashanthi, G. Thakur, T. Thundat, *Surf. Sci.* **606**, L83 (2012)
16. L. Hens, C. Block, J.J. Cabello-Eras, A. Sagastume-Gutierrez, D. Garcia-Lorenzo, C. Chamorro, K. Herrera Mendoza, D. Haeseldonckx, C. Vandecasteele, *J. Clean. Prod.* **172**, 3323 (2018)
17. N.A.I. Md Ishak, S.K. Kamarudin, S.N. Timmiati, *Mater. Res. Express.* **6**, 112004 (2019)
18. Y. Wang, D. O'Connor, Z. Shen, I.M.C. Lo, D.C.W. Tsang, S. Pehkonen, S. Pu, D. Hou, *J. Clean. Prod.* **226**, 540 (2019)
19. S.P. Patil, R.Y. Chaudhari, M.S. Nemade, *Talanta Open.* **5**, 100083 (2022)
20. A. Rana, A. Kumari, A.K. Chaudhary, R. Srivastava, D. Kamil, P. Vashishtha, S.N. Sharma, *Physchem.* **3**, 125 (2023)
21. A. Indriyani, Y. Yulizar, R. Tri Yunarti, O.B. Apriandanu, R.M. Surya, *Appl. Surf. Sci.* **563**, 150113 (2021)
22. F.J. Díaz López, C. Montalvo, *J. Clean. Prod.* **102**, 30 (2015)
23. X.H. Zheng, P.J. Chen, N. Ma, Z.H. Ma, D.P. Tang, *J. Mater. Sci.: Mater. Electron.* **23**, 990 (2012)
24. G. Biasotto, A.Z. Simões, C.R. Foschini, M.A. Zaghete, J.A. Varela, E. Longo, *Mater. Res. Bull.* **46**, 2543 (2011)
25. K.A. McDonnell, N. Wadnerkar, N.J. English, M. Rahman, D. Dowling, *Chem. Phys. Lett.* **572**, 78 (2013)
26. P. Scherrer, *Nachr. Ges. Wiss. Göttingen* **26**, 98 (1918)
27. J.I. Langford, A.J.C. Wilson, *J. Appl. Crystallogr.* **11**, 102 (1978)
28. V. Uvarov, I. Popov, *Mater. Charact.* **85**, 111 (2013)
29. F. Bhadala, L. Suthar, P. Kumari, M. Roy, *Mater. Chem. Phys.* **247**, 122719 (2020)
30. Z.B. Ayala, J. Peñalva, J.M. Hernández, H. Loro, C. Eyzaguirre, *J. Phys.: Conf. Ser.* **1558**, 012010 (2020)
31. M. Sakar, S. Balakumar, P. Saravanan, S.N. Jaisankar, *Mater. Design.* **94**, 487 (2016)
32. Y. Jiang, H. Ning, J. Yu, *AIP Adv.* **8**, 125334 (2018)
33. Z. Liu, Y. Qi, C. Lu, *J. Mater. Sci.: Mater. Electron.* **21**, 380 (2010)
34. F. Gao, X.Y. Chen, K.B. Yin, S. Dong, Z.F. Ren, F. Yuan, T. Yu, Z.G. Zou, J.-M. Liu, *Adv. Mater.* **19**, 2889 (2007)
35. P.S.V. Mocherla, C. Karthik, R. Ubic, M.S. Ramachandra Rao, C. Sudakar, *Appl. Phys. Lett.* **103**, 022910 (2013)
36. H. Ke, W. Wang, Y. Wang, J. Xu, D. Jia, Z. Lu, Y. Zhou, *J. Alloys Compd.* **509**, 2192 (2011)
37. R. Dhanalakshmi, M. Muneeswaran, P.R. Vanga, M. Ashok, N.V. Giridharan, *AIP Conf. Proc.* **1665**, 130014 (2015)
38. K. Abdelmadjid, F. Gheorghiu, B. Abderrahmane, *Materials.* **15**, 961 (2022)
39. S.H. Han, K.S. Kim, H.G. Kim, H.-G. Lee, H.-W. Kang, J.S. Kim, *Ceram. Int.* **36**, 1365 (2010)
40. I.S. Vijayashree, P. Niranjana, G. Prabhu, V.V. Sureshbabu, J. Manjanna, *J. Cluster Sci.* **28**, 133 (2017)
41. O.P. Bajpai, J.B. Kamdi, M. Selvakumar, S. Ram, D. Khashtgir, S. Chattopadhyay, *Express Polym. Lett.* **8**, 669 (2014)
42. S. Kossar, R. Amiruddin, A. Rasool, N.V. Giridharan, D. Dhayanithi, *Superlattices Microstruct.* **148**, 106726 (2020)
43. N.M.-R. Alikhanov, M.K. Rabadanov, F.F. Orudzhev, S.K. Gadzhimagomedov, R.M. Emirov, S.A. Sadykov, S.N. Kallaev, S.M. Ramazanov, K.G. Abdulvakhidov, D. Sobola, *J. Mater. Sci.: Mater. Electron.* **32**, 13323 (2021)
44. S. Bharathkumar, M. Sakar, M. Navaneethan, J. Archana, *Mater. Lett.* **304**, 130475 (2021)
45. S. Bharathkumar, M. Sakar, S. Balakumar, *J. Phys. Chem. C* **120**, 18811 (2016)
46. T. Karnan, S. Samuel, *Ceram. Int.* **42**, 4779 (2016)
47. D. Kumar, N. Lashari, T. Ganat, M. Abdalla Ayoub, A. Soomro, T.A. Chandio, *J. Mol. Liq.* **353**, 118821 (2022)
48. N.R. Niloy, M.I. Chowdhury, M.A.H. Shanto, J. Islam, M.M. Rhaman, *IOP Conf. Ser.: Mater. Sci. Eng.* **1091**, 012049 (2021)
49. A.M. Taiwo, O.R. Oladotun, A.M. Gbadebo, W.O. Alegbeleye, T.M. Hassan, *Environ. Monit. Assess.* **194**, 237 (2022)
50. H. Wu, P. Xue, Y. Lu, X. Zhu, *J. Alloys Compd.* **731**, 471 (2018)

**Publisher's Note** Springer Nature remains neutral with regard to jurisdictional claims in published maps and institutional affiliations.

Springer Nature or its licensor (e.g. a society or other partner) holds exclusive rights to this article under a publishing agreement with the author(s) or other rightsholder(s);

author self-archiving of the accepted manuscript version of this article is solely governed by the terms of such publishing agreement and applicable law.